

Supporting Information

Exploring Electronic Structure and Order in Polymers via Single-Particle Microresonator Spectroscopy

Erik H. Horak,[†] Morgan T. Rea,[†] Kevin D. Heylman,[†] David Gelbwaser-Klimovsky,[‡] Semion K. Saikin,[‡] Blaise J. Thompson,[†] Daniel D. Kohler,[†] Cassandra A. Knapper,[†] Wei Wei,[§] Feng Pan,[†] Padma Gopalan,^{†,§} John C. Wright,[†] Alán Aspuru-Guzik,[‡] and Randall H. Goldsmith^{†}*

[†]Department of Chemistry, University of Wisconsin-Madison, Madison, WI 53706, USA.

[‡]Department of Chemistry and Chemical Biology, Harvard University, Cambridge, Massachusetts, 02138, USA

[§]Department of Materials Science and Engineering, University of Wisconsin-Madison, Madison, WI 53706, USA.

*E-mail: rhg@chem.wisc.edu

1 Single-Particle Spectroscopy

AFM of Single Particles of PEDOT:PSS The relevance of single-particle spectroscopy to the properties of bulk materials requires justification, especially as the deposition conditions require a substantially lower concentration than typically used to make conductive PEDOT:PSS films. We have investigated the possible morphological differences produced by our deposition conditions and found a high degree of similarity to our single-particle conditions and bulk conditions.

A critical consideration for PEDOT:PSS is the particle-like nature of the aqueous dispersion. Unlike many conjugated polymers that are deposited from solvents that completely solubilize the polymer species, PEDOT:PSS is cast from a colloidal suspension. This difference is due to the two-component nature of PEDOT:PSS, where one specific role of the PSS is to make a water-soluble dispersion. This dichotomy gives rise to phase segregation of PEDOT:PSS particles with a PEDOT rich core and a PSS rich shell (see text). During film deposition, these suspended particles assemble to form the thin film, but the “character” of the particle is largely preserved in the process. Thus the films created can be thought of as a conglomeration of many PEDOT:PSS particles where the precise deposition method does not drastically alter the internal structure of each particle. Conspicuous evidence of this preservation can be seen in TEM images of PEDOT:PSS by Ruit et al.¹ They observe nano-fibrils in vitrified solutions, essentially examining the aqueous dispersion morphology before deposition (Figure S1d), and then after deposition they observe highly similar fibrils in thin conductive films (Figure S1e), suggesting minimal morphological alteration during deposition. These one-dimensional structures have also been seen

in other reports. TEM measurements by Lee and coworkers³ specifically take note of these fibrils

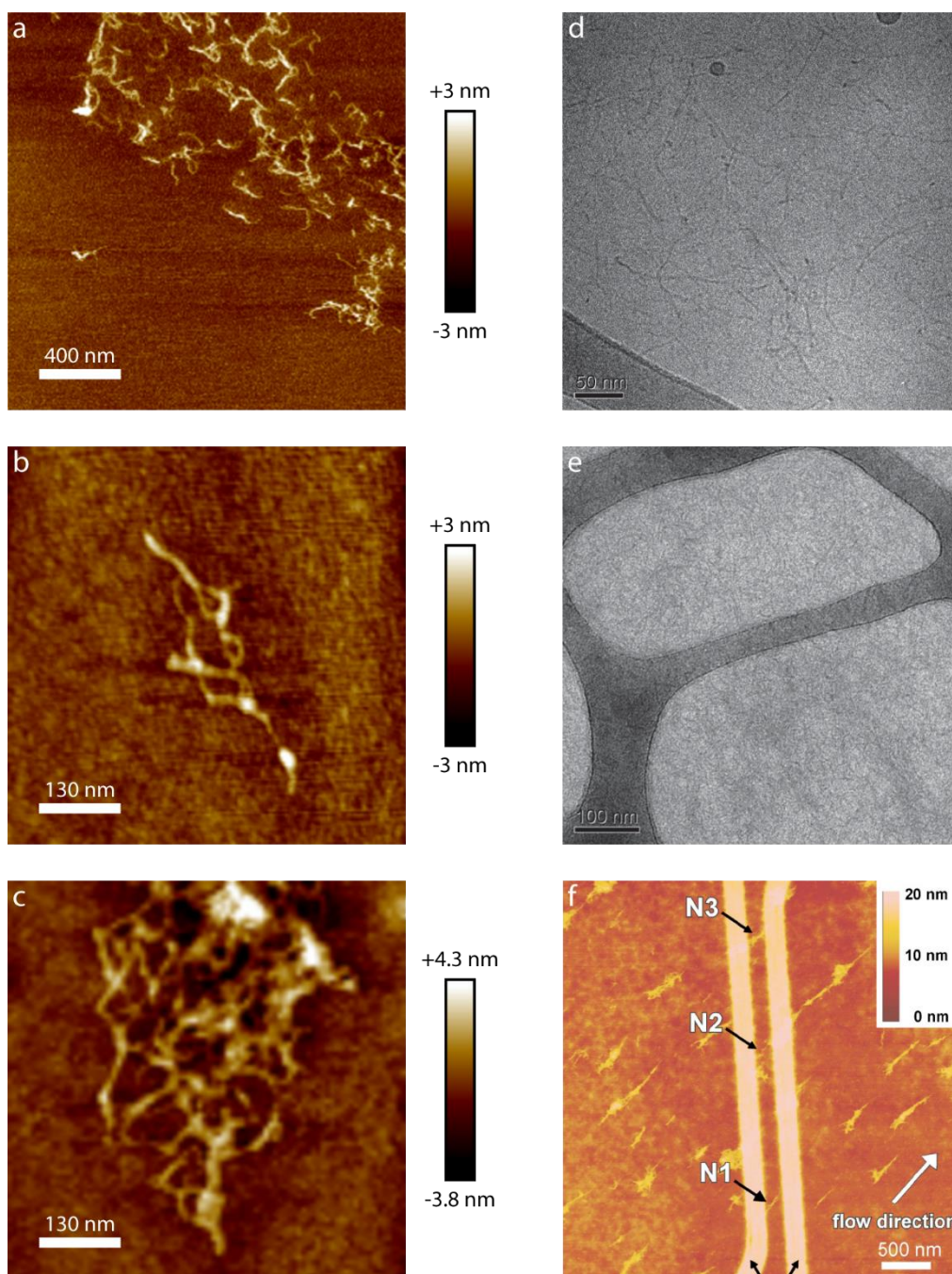


Figure S1: AFM and TEM images of single PEDOT:PSS particles. (a) AFM height map of PEDOT:PSS deposited on a silicon substrate at 100 $\mu\text{g/mL}$. (b-c) AFM height map of PEDOT:PSS deposited on the rim of the toroidal optical microresonator at 1 and 10 $\mu\text{g/mL}$ respectively. (d) Cryo-TEM image of a vitrified PEDOT:PSS solution examining the morphology of PEDOT:PSS in the aqueous dispersion.¹ (e) High resolution TEM image of a PEDOT:PSS film from the same solution as (d) on a TEM grid (light and dark colors).¹ (f) AFM height maps of single PEDOT:PSS nanofibrils deposited under flow.²

during their investigation of acid treated PEDOT:PSS films (the highest PEDOT:PSS conductivity to date). They also find these fibrils in high-angle annular dark-field scanning transmission electron microscopy. While the fibrils are most conspicuous for their most conductive films, they are also visible in the TEM of the pristine films. Further, AFM phase images have revealed phase segregation into PEDOT-rich and PSS-rich regions, with the PEDOT-rich grains forming networks of elongated structures^{4, 5} reminiscent to that of a network of fibrils. Samitsu et al have also seen fibrils in highly dilute conditions and were able to measure the conductivity of these individual fibers,² Figure S1f. Importantly, the temperature dependence of bulk PEDOT:PSS film conductivity displays approximately one-dimensional hopping behavior¹ suggesting that the base unit of the film is indeed these conductive fibrils. Thus, PEDOT:PSS films can be viewed as interwoven nano-fibrils of PEDOT:PSS, where each particle is kinetically trapped in states very similar to that in solution.

To assess any morphological differences due to the conditions used in our experiment, we have undertaken AFM measurements both on a flat silicon substrate (Figure S1a) and directly on the toroidal optical microresonators (Figure S1b,c) we use to perform spectroscopy. The on-toroid measurements entail deposition from a PEDOT:PSS solution of ~50x our typical single-particle conditions. However, these measurements are still in a highly dilute regime and the elevated concentration was necessary as we are only able to image part of the toroid. In these measurements we find nano-fibrils both on the silicon substrate and on the resonator, highly reminiscent of previous single-particle AFM measurements of PEDOT:PSS,² Figure S1f. These findings suggest that the morphology of the particles we are analyzing in our optical experiment is similar to the morphology that is typically found under deposition conditions that yield conductive films. Taken together, our evidence suggests that we are simply interrogating the relatively unaltered particles

of PEDOT:PSS that deposit intact from solution that also make up the fundamental one-dimensional conductive unit in a conductive PEDOT:PSS thin film. Thus, we have shown that the single particles that we are examining in our work are morphologically, easily recognizable and fundamental pieces in the bulk films, conspicuous evidence that our single-particle targets are a highly relevant architectural motif in the structure of the bulk film with a strong connection to conductivity.

Further, the size of these objects is also consistent with our optical signals. We observe identifiable single nanofibrils of PEDOT:PSS ranging from ~30-300 nm and interwoven strands forming aggregates considerably larger. These objects are also quite flat, typically 2-3 nm in height, and are typically 8-15 nm wide. These sizes roughly match the sizes already found in the literature.¹⁻³ Using these estimates, 1.45 g/cm³ as the density of the polymer,⁶ a molecular weight of 400,000 g/mol PSS,⁷ a weight ratio of 1:2.5 PEDOT:PSS,⁷ and assuming an elliptical cylinder for a geometry, we find that the range of observed sizes of a single nanofibril will include 0.6-16.5 PSS strands decorated with PEDOT oligomers. The value, 0.6 PSS strands, simply suggests a strand that is shorter than an average PSS strand. Importantly, this range of sizes from the AFM measurements matches the range of sizes inferred from our optical measurements, which suggest on the order of 1 PSS strand. In addition, this range of values further demonstrates the highly heterogeneous nature of PEDOT:PSS, even at the level of individual particles. The AFM-derived nanofibril composition of 0.6-16.5 PSS strands translates into a range of absorption cross-sections of 4×10^{-14} to 1.1×10^{-12} cm², which is why even a single nanofibril can have a range of values, consistent with Main Text Figure 2a. Thus, even with this heterogeneity, we achieve qualitative agreement between the estimates from our optical signals (see main text) and AFM measurements.

Relevance of Deposition Conditions In our experiment we deposit PEDOT:PSS via spin-coating at 4000 rpm. The PEDOT:PSS literature contains examples of many deposition parameters from drop-casting to spin coating at 6000 rpm, all creating conductive films. It is fairly typical to use variable spin-coating speeds to control film thickness. Specifically, in the work of Matolli and coworkers⁸ they examine the conductivity of a PEDOT:PSS sample upon varying film thickness controlled via spin coating velocity. They vary the spin coating velocity from 1000-6000 RPM achieving film thicknesses ~40-130 nm thick and see only minor changes of conductivity, suggesting our results from 4000 RPM are representative.

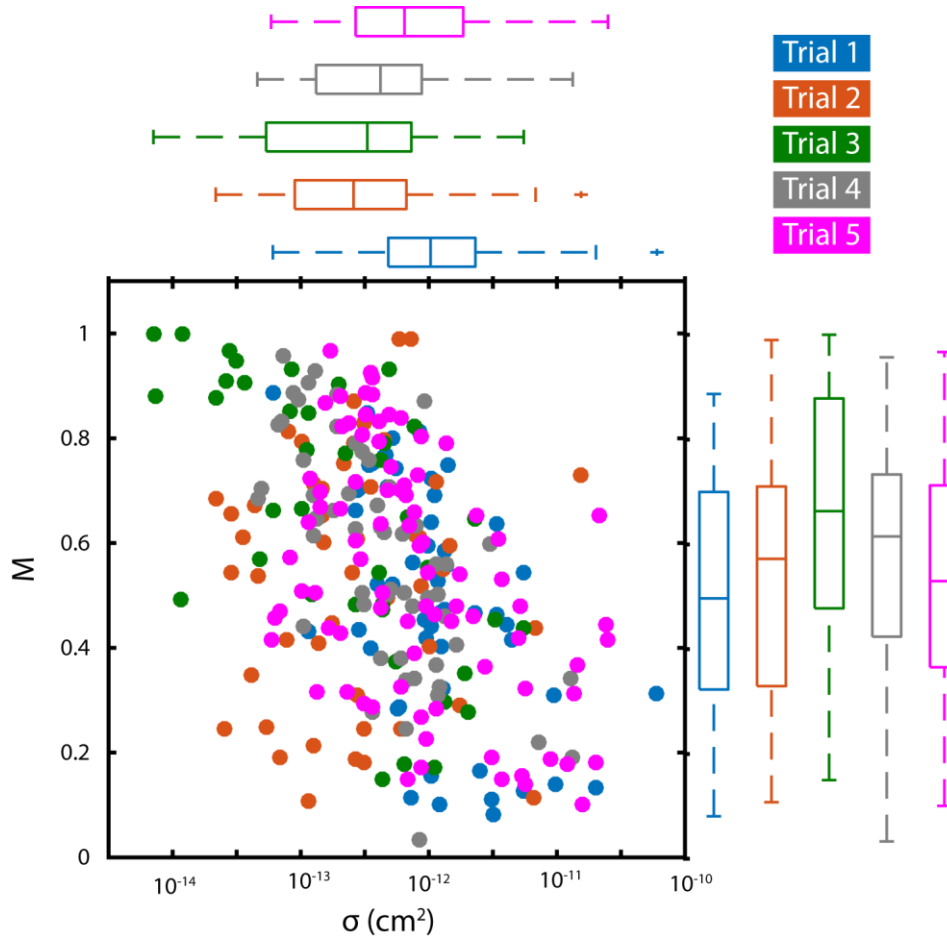


Figure S2: Single-particle trial variability. Correlation between the absorption cross-section (σ_{abs}) and depth of modulation (M) along with box and whiskers plots of σ_{abs} and M along for all 5 trials of single-particle measurements of PEDOT:PSS.

Variability in Data Sets The single-particle spectroscopy data set was taken by examining particles on many individual toroids in 5 independent trials. Each trial consisted of a different microresonator chip (set of microresonators), and different solution of PEDOT:PSS made at different times. Some trial to trial variability was observed in both absorption cross-section (σ_{abs}) and depth of modulation (M), depicted in Figure S2. The origin of this variability could stem from a number of different sources, including deposition concentration, toroid cleaning procedure, time elapsed from toroid cleaning, sample aging, and spin-coating acceleration conditions. The correlation between σ_{abs} and M featured in Main Text Figure 3, however, was preserved through all trials.

Radial Deposition Distribution During sample characterization, the objects were binned to 4 different locations of the toroid (Figure S3a): outer rim, inner rim, interstitial, and pillar edge. As can be seen in Figure S3b, the conditions used to deposit PEDOT:PSS onto the toroidal

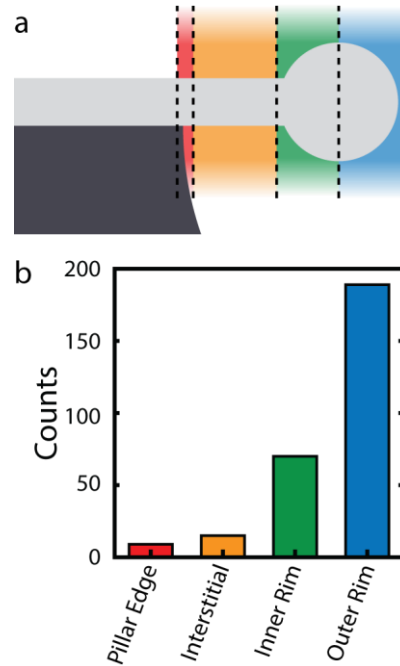


Figure S3: Radial position of deposition. (a) Different binned positions of deposited objects on the toroidal resonator. (b) Number of objects experimentally found at each binned location.

resonator yielded a selective placement of objects, 259 out of 283, on the outer rim or inner rim of the toroid. This detail is important for 1) the sensitivity of the measurement—as it provides a better overlap of the photothermal plume with the WGM of the resonator⁹ allowing for objects as small as $8 \times 10^{-15} \text{ cm}^2$ to be detected, and 2) the surface normal experienced by the majority of the objects is not parallel to the optical axis of the pump beam—allowing for the surface angle determination described in the Main Text. This selective deposition is quite favorable and we are currently exploring methods to understand and control this deposition.

Smallest Object The smallest object experimentally observed had a σ_{abs} of $8 \times 10^{-15} \text{ cm}^2$. The photothermal map (Figure S4a) reveals a small object on top of a large photothermal background arising from absorption by the microresonator itself, most likely water residing in the glass from the fabrication process as the absorption rises to the red edge of our spectral window corresponding to water's vibrational overtone.⁹ The polarization dependence of this object, seen in Figure S4b, vanishes after background subtraction, suggesting a well oriented and crystalline PEDOT:PSS particle. While the spectral response of this object appears to be slightly peaked (Figure S4c), this non-flat response may be in part due to the varying power of our pump beam as

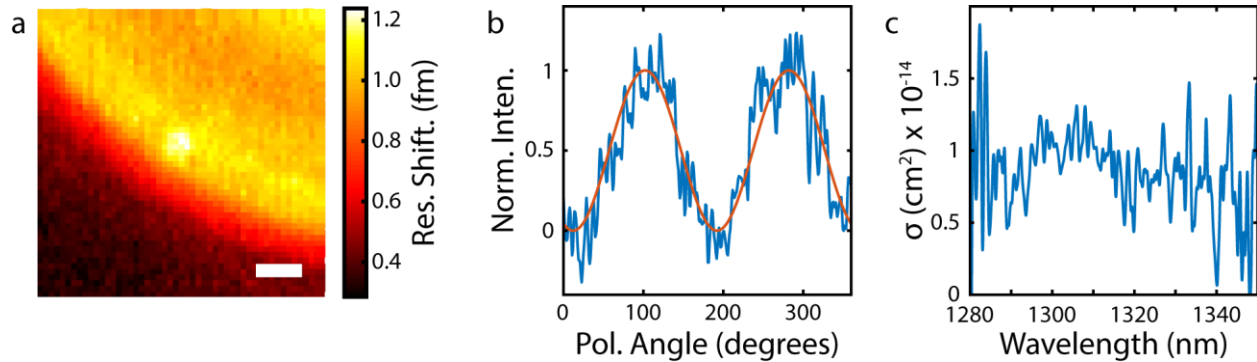


Figure S4: Smallest object data set. (a) The photothermal map of the smallest object, visible on top of the large photothermal background of the resonator. (b) Polarization dependence of the smallest object in blue with a sinusoidal fit to the data with extinction of the signal observed or a unity value for depth of modulation ($M=1$). (c) Absorption spectra of the smallest object.

a function of wavelength, with the peak of the object roughly corresponding to the peak power of the pump laser. Further, on the red edge of our spectral window the background absorption increases dramatically, reducing the signal to background ratio and complicating background subtraction. Thus at wavelengths further away from 1300 nm the signal to noise significantly decreases due to reduced pump power, prohibiting a definitive identification of discrete spectral feature, though this is not a fundamental limitation of our microresonator-based spectrometer. The value of $8 \times 10^{-15} \text{ cm}^2$ was extracted at 1315 nm, the wavelength that the photothermal map and polarization data was acquired.

Single PEDOT:PSS Polymer Assessment To estimate the cumulative σ_{abs} of the many PEDOT oligomers decorating a single PSS chain, i.e. a single PEDOT:PSS polymer, many materials properties of PEDOT:PSS were gathered, summarized in Figure S5. The molecular-weight⁷ of PSS was assumed to be ~400,000 g/mol and a PEDOT:PSS weight ratio⁷ was assumed to be ~2.5:1. This yields ~160,000 g PEDOT/mol PSS, and given the EDOT monomer molecular-weight, this gives a value of ~1140 EDOT monomers/PSS strand. Then using a value of 7 monomers per bipolaron for a similar polythiophene,¹⁰ which is in good agreement with the ~30% doping reported for PEDOT:PSS,¹¹ provides an estimate of 160 bipolarons/PSS strand. Finally, with the per-bipolaron absorption constant of a doped polythiophene¹⁰ ($4.2 \times 10^{-16} \text{ cm}^2$) this can be directly converted to $6.7 \times 10^{-14} \text{ cm}^2$ for a single PEDOT:PSS polymer. The value of $4.2 \times 10^{-16} \text{ cm}^2$ used in our calculation is a three-fold larger value than that reported in the text of Ref. 3, as their measurement was that of a bulk disordered system where chromophores are randomly oriented in 3D¹² while our model applies to a single chromophore favorably oriented in 1D (see Supporting Information Section 2:Model Explanation and Analysis for further discussion). Also given that

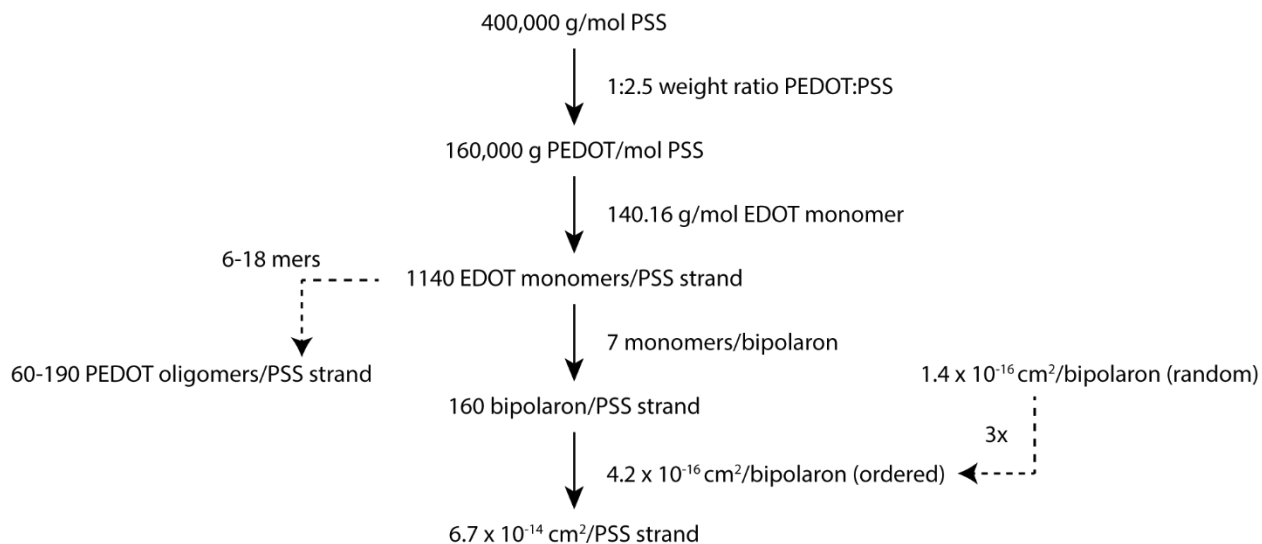


Figure S5: Single PEDOT:PSS polymer assumptions. Calculation and assumptions for a quantitative estimate of σ_{abs} of a single PSS strand decorated with many PEDOT oligomers, referred to as a single PEDOT:PSS polymer.

each PEDOT oligomer consists of 6-18 mers,¹³ then there exists between 60 and 190 PEDOT oligomers/PSS molecule. Thus, each PEDOT oligomer can be assumed to contain one bipolaron.

One possible source of deviation from the above calculations is a PEDOT:PSS weight ratio of 1.5:1 or 1.8:1, due to a disparity between film and solution values,¹⁴ most likely caused by excess PSS completely phase segregating from the PEDOT:PSS film.¹⁵ Another origin of deviation from the above calculations is in the value of the bipolaron absorption constant. A different method determined the polaron optical constant for another polythiophene¹⁶ and found a value of $4 \times 10^{-16} \text{ cm}^2$ (disordered), but relied on electrical doping and thus is less relevant to the chemically doped material studied in here. If both of these alternative values are used, then the σ_{abs} of a single PEDOT:PSS polymer is calculated to be $3.2 \times 10^{-13} \text{ cm}^2$ and consist of ~ 270 bipolarons per PSS strand (both alternate values push the number of bipolarons to larger quantities) instead of $6.7 \times 10^{-14} \text{ cm}^2$ and 160 bipolarons. This shift also changes the number of PEDOT oligomers associated with the 50% falloff of chromophore alignment (β) to 1400 oligomers instead of 3950. Importantly, none of these shifts alter the main results of our work that include the observation of spectra from

individual PEDOT:PSS polymers that resemble bulk spectra, or the observation of long-range PEDOT ordering.

Homogeneous Linewidth in Single-particle Spectra and Limits of a Finite Spectral Window To quantitatively determine a lower limit for the homogeneous linewidth of a bipolaron in the single-particle spectra we employed a Fourier transform-based comparison of the experimental and calculated spectra, Figure S6. First the simulated spectra were created. The simulated energies were broadened with Lorentzians of the specified homogeneous linewidth along with the two added side peaks associated with the vibronic progression from a similar polythiophene,¹⁷ where the peaks in the vibronic progression were 0.16 and 0.32 eV blue-shifted from the calculated peak and of relative intensity of 0.45 and 0.2 from the main peak, respectively. This vibrational progression serves to further smooth out the spectrum. The spacing is a reasonable estimate for PEDOT:PSS which shows a similar Raman spectrum to the polythiophene.¹⁸ Prior to taking the Fourier transform, both the experimental and calculated spectra were normalized such that the integrated area was unity. In this way the y-axis of both the absorption spectrum and Fourier spectrum describes the proportion of the absorption spectrum at a given wavelength or spatial frequency, respectively. The Fourier spectrum of the calculated spectra all produce simple monotonically decreasing Fourier intensities with increasing spatial frequencies, as the overlap between broad randomly distributed Lorentzian features and the sinusoidal waveforms decreases with increasing spatial frequency of the sinusoid. Said another way, the slow undulations in the absorption spectra are better represented with low spatial frequencies than with higher ones. Thus as the homogeneous broadening increases, the Fourier intensity curves shift downwards and the spectral undulations are even slower. The experimental spectra show a similar Fourier spectra with an additional feature, a broad shoulder at higher spatial frequencies as a result of experimental

noise. The contribution of the noise increases for smaller values of σ_{abs} as the S/N ratio of our experiment decreases. The slow spatial frequencies, however, still report on the slow undulations of spectral features and thus offer a direct comparative measure of the relative smoothness of the experimental and calculated spectra. In this way the homogeneous linewidth of the single-particle measurements was found to be >70 meV, in qualitative agreement with the simulated spectra in Main Text Figure 2c.

It is important to note that while our spectral window is limited to a specific energy range, if discrete absorption features existed that overlapped even partly with our spectral window, we would be able to resolve features with our spectrometer, as we have observed linewidths of 68 meV for plasmonic gold nanorods,⁹ including seeing slopes associated with the tails of features whose center lies outside of our spectral range. Such slopes are not observed here.

However, it is worthwhile to analyze the possibility that our flat observed spectra originate as a tail of peaked feature that exists outside of our observation window. A more quantitative measure of our ability to detect these features employs a similar Fourier analysis described above to determine the linewidth. We examined the expected response in our limited wavelength region

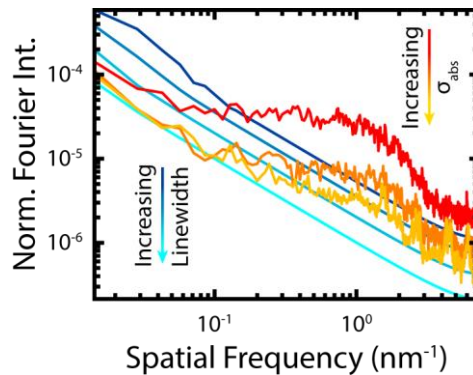


Figure S6: Fourier transform analysis to determine homogeneous linewidth. The Fourier intensities of the experimental single particle spectra with increasing values of σ_{abs} , in red ($<1 \times 10^{-14.5} \text{ cm}^2$), orange ($\sim 1 \times 10^{-13.5} \text{ cm}^2$), and yellow ($\sim 1 \times 10^{-13} \text{ cm}^2$), and calculated spectra of increasing homogeneous linewidth, in blues (10, 20, 40, and 80 meV).

from a Lorentzian feature both blue- and red-shifted outside of our spectral window with varied linewidths in the presence of noise. An example is shown in Figure S7a, where the linewidth is varied around a feature centered at 1400 nm (50 nm red-shifted outside of our spectral window). Gaussian noise is added to this simulated spectrum with an amplitude comparable to our experimental noise. The Fourier transform of spectra were then taken as described above. The example spectra in Figure S7a resulted in the Fourier transformed data in Figure S7b. Fourier transformed spectra were then compared to the experimental Fourier transformed data. To avoid the interference of experimental noise and to compare the slow spatial frequencies we directly compare the 7 smallest frequencies of the Fourier transforms (the diamonds in Figure S7b). Clearly the example spectra have higher Fourier intensity than the experimental data (Figure S7b) and thus we reject the possibility of a spectral feature at 1400 nm with a linewidth < 200 meV. We repeat this for many different center wavelengths and linewidths with the comparison between simulated and experimental spectra represented in Figure S7c. Here the colorbar represents the fraction of the 7 compared points where the simulated spectra are higher than the experimental spectra, where if 7/7 simulated points (yellow) are above the experimental data then we reject the wavelength and linewidth as a possible location of a spectral feature, whereas if 0/7 simulated points (blue) are above the experimental data we cannot rule out the existence of a spectral feature at this location. Intermediate values (teal) represent marginal cases with some uncertainty. Thus the yellow area in Figure S7c represents the area where it is unlikely a spectral feature would exist and we can safely say there is no spectral feature between ~ 1050 - 1800 nm with a linewidth of < 200 meV.

Intuitively, the size and linewidth of a peak outside of our spectral range would also impact our ability to resolve it. The red and black line in Figure S7c corresponds to situations where a peak with 20x and 100x maximum intensity relative to our observed feature in our spectral window

exists outside of our observation window. Within the 20x bounds (in between the red curves) the vast majority of the area is yellow suggesting it is highly unlikely that there exists a spectral feature outside our wavelength range, as we would detect it as an elevation of the lower spatial frequencies. If the peak is 100x larger (between the black curves) much of the area is also yellow. However, if

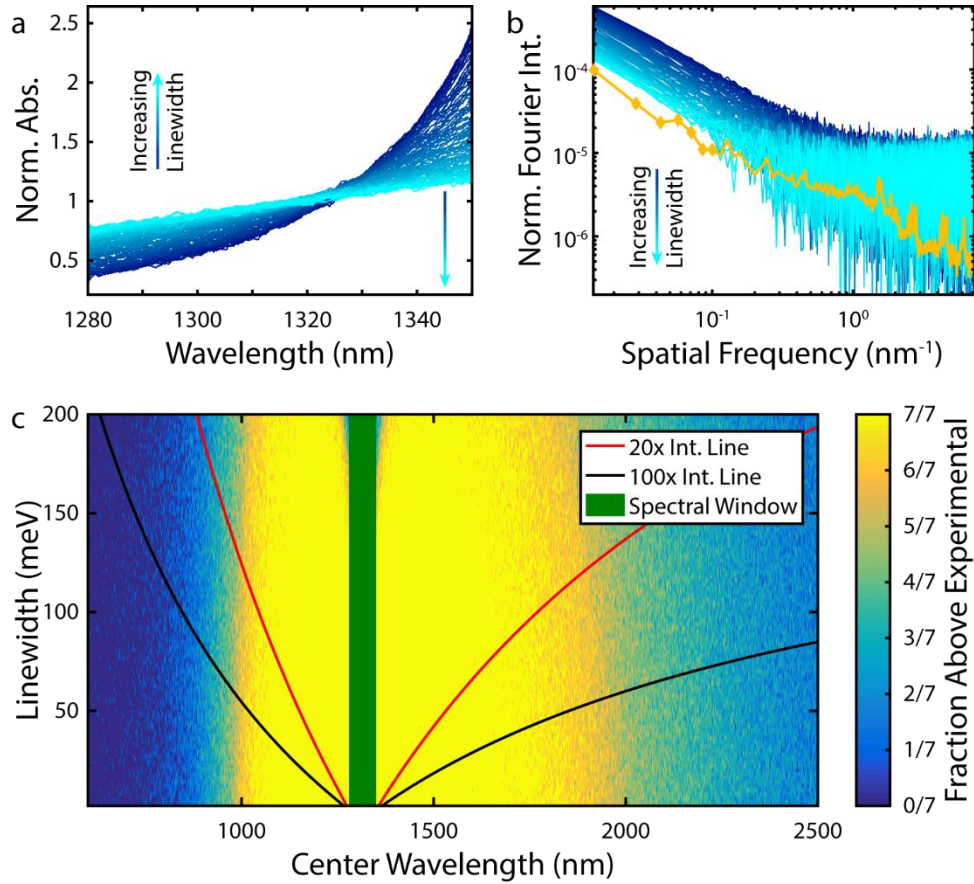


Figure S7: Limited spectral window analysis. (a) Predicted spectra inside the spectral window for a Lorentzian feature at 1400 nm with linewidths varying from 2-200 meV. Each spectra is normalized to the integrated intensity in the spectral window. (b) Fourier transforms of these example spectra from (a) alongside an experimental Fourier transform (yellow), with the 7 smallest spatial frequencies represented in diamonds. (c) Comparison of the experimental and simulated Fourier transforms at many center wavelengths and linewidths outside the experimental spectral window (green box). A higher fraction of the 7 spatial frequencies of the simulated spectra above the experimental spectra indicates a reduced likelihood of a spectral feature with those parameters. The relative intensity ratio of the peak intensity of a spectral feature compared to the intensity in the spectral window is depicted in the red and black lines, 20x and 100x respectively. Features in the yellow region of (c) would be easily observable and are thus easily discounted. Features existing in blue regions would be difficult to discern, but are unlikely (see text).

the feature is quite broad and centered far from our observation window, we would have difficulty discerning this from our observed spectra, an intuitive result as in such a case the spectra would appear flat. However, we can disregard the possibility of a spectral peak blue-shifted further than ~900 nm with >100 meV as this seems unphysical for bipolaron absorption features in PEDOT oligomers, a material that is transparent in the visible. Similarly, a substantially redshifted spectra is also unlikely, as electronic absorption in this region would require a significantly delocalized transition, which is unlikely in a disordered material. Thus while we cannot completely rule out discrete absorption features substantially shifted from our spectral window, given our high spectral sensitivity and physical constraints, the probability of such a feature existing seems highly remote.

In summary, our analysis indicates that the likelihood that our flat absorption is as a result of a spectrally distant spectral feature is very small. We thus focus on the origin of our spectrally flat response as arising from many spectral features as described by our computational analysis in the main text. Future experiments employing a more broadly tunable pump source and thus larger spectral range, and smaller objects with less heterogeneous broadening, are in progress.

Contribution of Spectral Diffusion and Charge Motion The spectra shown in Main Text Figure 2b are acquired over approximately 80 seconds. Thus linewidths are also influenced by slower fluctuations of the energy of the spectral features, such as spectral diffusion. Spectral diffusion has been observed in a variety of systems consisting of dye molecules embedded in a polymer matrix or proximal to a surface at room temperature,^{19, 20} a highly comparable environment to our PEDOT:PSS sample. Spectral diffusion behavior can be either excitation power dependent or independent.¹⁹ Mechanisms of power-dependent spectral diffusion, such as non-photochemical hole burning that rely on evolution of the coupled chromophore-lattice in the

excited state are likely not at play due to the extremely short excited state lifetime of our system. On the other hand, power-independent spontaneous spectral diffusion may be a contributor. Examination of several previous reports of spectral diffusion in a variety of host-guest systems suggest spectral diffusion resulting in a contribution to the FWHM of the observed line shape of up to 20 meV.¹⁹⁻²¹ Rare large-magnitude spectral jumps have also been seen in single-molecule fluorescence measurements.²⁰ While we cannot completely rule out such large jumps in our absorption spectroscopy, they would likely manifest as abrupt changes in signal intensity during acquisition of electronic absorption or polarization spectra, which were not observed.

Other reports of spectral diffusion arise from enhanced Stark shift due to proximal injection of charges creating large nearfield electric fields.^{22, 23} Room temperature measurements find trapped charges in the polystyrene host reversibly shift fluorescence spectra by $<300\text{ cm}^{-1}$ ($<37\text{ meV}$) on a timescale of roughly $\sim 100\text{ ms}$. Thus, this source of spectral diffusion seemingly may be an important interfering influence in our analysis. However, as the charge carriers move considerably faster in this conductive material,^{24, 25} these energy fluctuations likely contribute to homogeneous broadening rather than spectral diffusion.

2 Modelling Crystallinity

Model Explanation and Validation The model described here is similar to that used to examine rotational diffusion of nanoparticles.²⁶ The procedure entails choosing an initial orientation in spherical coordinates dictated by a random θ chosen from a square distribution from 0 to 360° , and a ϕ chosen from a square probability distribution in $\sin(\phi)$. A Cartesian unit vector, representing a single bipolaron chromophore and effectively normalizing the model intensity to $4.2 \times 10^{-16}\text{ cm}^2$ (see Supporting Information Section 1: Single PEDOT:PSS Polymer Assessment),

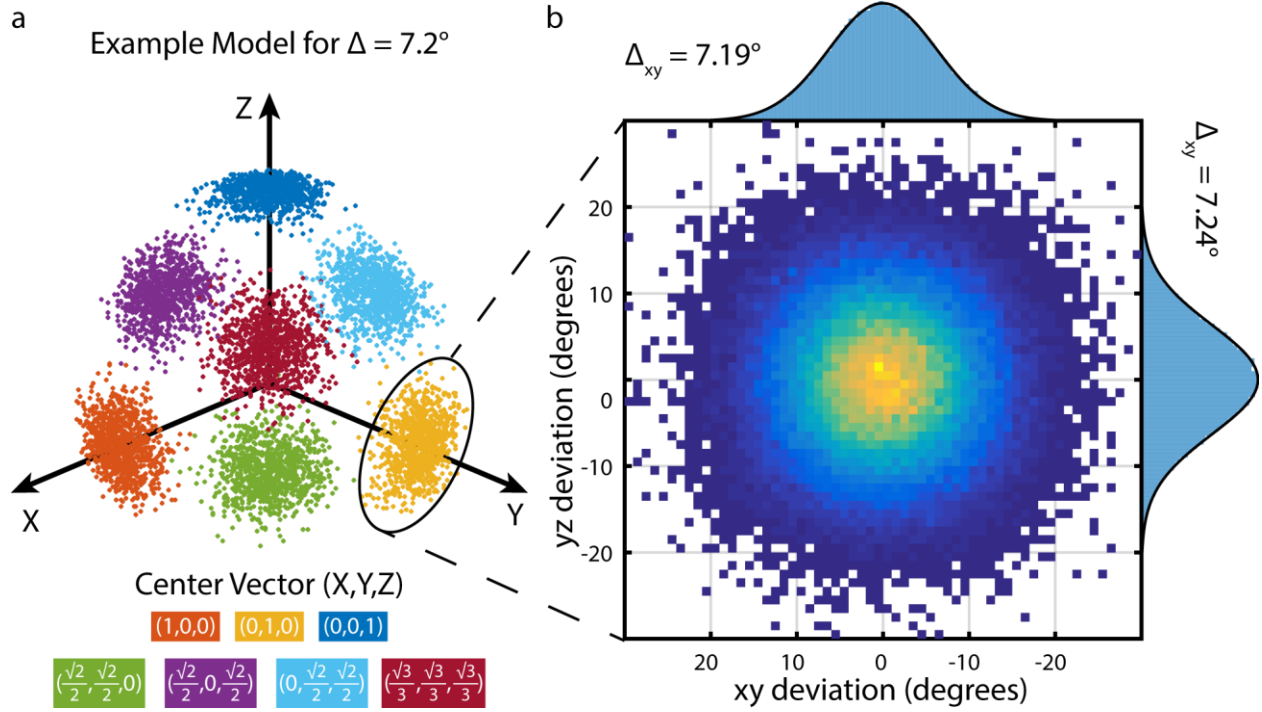


Figure S8: Rotational model validation. (a) Example random rotations about different initial vector coordinates for an example Δ of 7.2° to show that these random rotations are general. (b) Angular distribution about an initial vector pointed along the y-axis, to show that this rotational model creates a distribution of the desired value of Δ .

was generated from these random values of θ and ϕ . A subsequent dipole was modeled by introducing random rotations of the previous dipole about the Cartesian coordinate system x (R_x), y (R_y), and z (R_z), Equation 4. The amount of rotation about each axis was determined by a Gaussian weighted number generator with a standard deviation of Δ , Equation 3.

$$\begin{bmatrix} x_{i+1} \\ y_{i+1} \\ z_{i+1} \end{bmatrix} = R_x(\Delta) R_y(\Delta) R_z(\Delta) \begin{bmatrix} x_i \\ y_i \\ z_i \end{bmatrix} \quad (3)$$

$$R_x(\Delta) = \begin{bmatrix} 1 & 0 & 0 \\ 0 & \cos \Delta & -\sin \Delta \\ 0 & \sin \Delta & \cos \Delta \end{bmatrix}, \quad R_y(\Delta) = \begin{bmatrix} \cos \Delta & 0 & \sin \Delta \\ 0 & 1 & 0 \\ -\sin \Delta & 0 & \cos \Delta \end{bmatrix},$$

$$R_z(\Delta) = \begin{bmatrix} \cos \Delta & -\sin \Delta & 0 \\ \sin \Delta & \cos \Delta & 0 \\ 0 & 0 & 1 \end{bmatrix} \quad (4)$$

The resulting orientation displacements produce a 2D Gaussian distribution centered about the original vector with a standard deviation of Δ and is generalizable to any original vector orientation, Figure S8a. The distribution of Figure S8a displays only the angular displacement, a similar deviation of cofacial alignment, where the parallel planes of two stacked molecules can rotate in the fixed cofacial geometry, is also expected.

This process was repeated for 10^7 random rotations of subsequent vectors, generating a single random walk. For each newly generated vector the 2D intensity distribution in the xy plane was calculated, as experimentally the polarization dependence only captures the 2D absorption orthogonal to the optical axis of the pump beam, Equation 5. The cumulative intensity after each dipole was also determined and represents the collective 2D intensity distribution of many oligomers, Equation 6.

$$I_i(\theta) = \sin^2(\varphi_i) \cos^2(\theta - \theta_i) \quad (5)$$

$$I_{\text{cumulative},i}(\theta) = \sum_1^i I_i(\theta) \quad (6)$$

From the cumulative 2D intensity distribution the maximum intensity and depth of modulation (M) were determined for each collection of chromophores. By multiplying the normalized intensity by the well-aligned per-bipolaron absorption constant, $4.2 \times 10^{-16} \text{ cm}^2$, the σ_{abs} and M value at every step in the random walk can be calculated, creating a M trajectory. This was repeated 100 times for a single value of Δ , a random collection of 5 trajectories are displayed in Figure S9a. From each of the 100 trajectories, a subset of points logarithmically spaced in the number of dipoles modeled were used to create a density distribution seen in Figure S9b. These points were also used to fit the model to a logistic function (see Main Text) and extract the characteristic alignment

falloff, β . The Main Text Figure 3e, is generated from these points but weighted with a Gaussian number generator with the mean and standard deviation observed in the experimental distribution

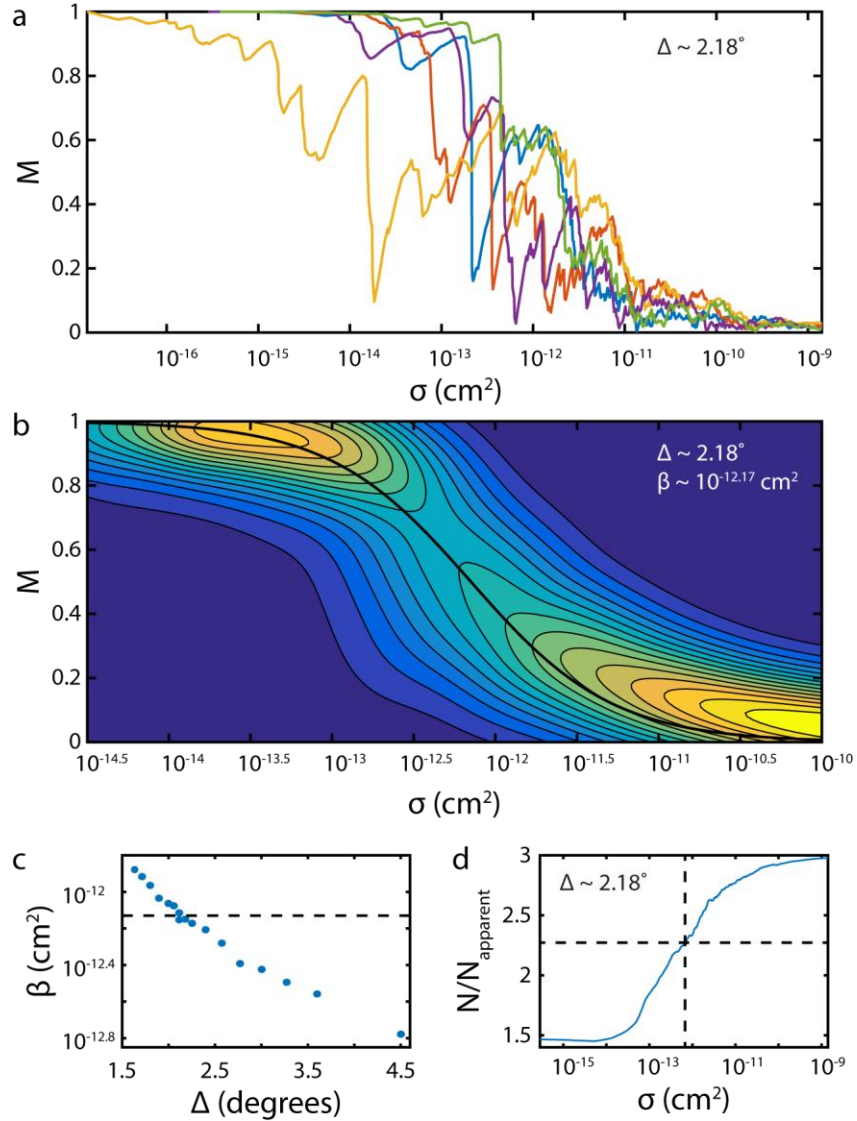


Figure S9: Example model and modeling parameters. (a) Example trajectories of depth of modulation (M) for a standard deviation of nearest neighbor angular deviation (Δ) of 2.18° . The yellow trace started with an orientation mostly oriented parallel to the modeled optical axis (orthogonal to the electric field) consequently starting at a small apparent absorption cross-section (σ_{abs}). (b) Density distribution of the modeled M -falloff data with an even logarithmic spacing of points without the Gaussian sampling to recreate the experimental distribution with a logistic equation fit in black. (c) Value of the σ_{abs} at 50% falloff of chromophores alignment (β) as a function of Δ in the rotational model, with the experimental value of β as a dashed line. (d) Examination of the ratio of actual number of chromophores to apparent number of chromophores (N/N_{apparent}) dependent upon σ_{abs} where if $\sigma_{\text{abs}} \sim \beta$, at the dashed crosshairs, then $N/N_{\text{apparent}} \sim 2.25$.

of σ_{abs} and finding model points points closest to the randomly generated σ_{abs} value. This process was repeated for many simulations with different values of Δ , thus finding the relationship between β and Δ (Figure S9c). In this way, the experimental β of $10^{-12.13} \text{ cm}^2$ was found to correspond to a simulated Δ of about 2.18° .

This model can also be used to estimate the number of oligomers probed experimentally. The largest objects experimentally examined have a small M suggesting a highly disordered system. Thus the measured intensity only provides a measure of the component of the chromophores oriented along a single axis and thus underestimates the total number of chromophores as a significant component of chromophores lie on orthogonal axes. To determine the total number of chromophores (N) from the apparent number of chromophores (N_{apparent}) a simple multiplier must be used. For a highly disordered object, essentially isotropic, the value of $N/N_{\text{apparent}} = 3$ as can be seen in Figure S9d for large σ_{abs} . The estimate of the number of oligomers in the largest object in the Main Text incorporates this value of 3. For small, highly-ordered objects, the value of N/N_{apparent} is highly variable depending upon the orientation of the anisotropic collection, with a minimum value of 1 when the object is oriented in the xy-plane and a value of ∞ when the object is oriented parallel to the z-axis, the optical axis. Integrating over all orientations

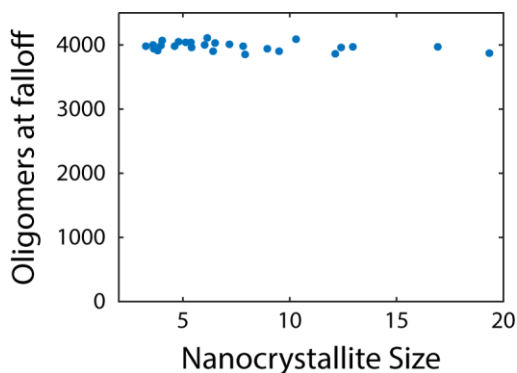


Figure S10: Effect of pre-organization. The estimated number of PEDOT oligomers at the modulation depth falloff is not dependent upon the number of PEDOT oligomers in the assumed nanocrystallite.

the expectation value of N/N_{apparent} is 1.5 and can be seen in Figure S9d as the limit for small objects. For objects at the characteristic falloff of β the value of $N/N_{\text{apparent}} \sim 2.25$ was used as this represents the middle ground between the two extremes above (Figure S9d). This value of 2.25 is used in the Main Text to determine the true number of oligomers at the experimental value of β .

Effect of Pre-organization The model described above uses single PEDOT oligomers as the base unit for rotational organization, however, PEDOT:PSS has been shown to contain small PEDOT nanocrystallites, with ~ 3 -4 oligomers in untreated films and ~ 13 -14 oligomers in the most conductive films. Thus perhaps a more appropriate base unit for this model is some small number of perfectly aligned oligomers forming the nanocrystallite, this can be readily achieved by simply assuming a different absorption cross-section for the single modelled dipole. While this alternative model certainly affects the angular deviation between the base units (for example the intra-aggregate ordering is assumed to be perfect, and the inter-aggregate ordering will be considerably less than the 2.2° with a base unit of one oligomer), it has only a marginal effect on the total number

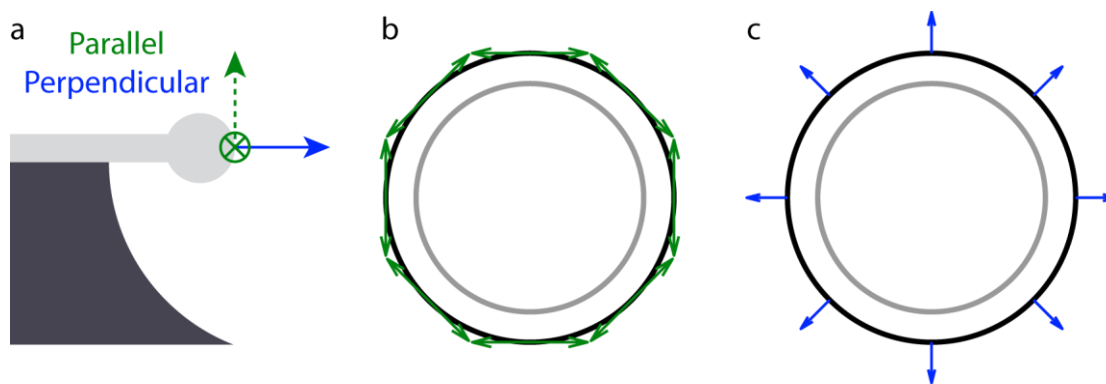


Figure S11: Relating polarization angle with radial coordinate. (a) Cartoon of the dipole surface orientation at the outer rim of the toroid, with parallel in green and perpendicular in blue. The dashed green arrow represents objects that are parallel to the optical axis and thus not visible in our experiment, we are much more likely to examine the objects orthogonal to the optical axis seen in the solid green cross. (b) Predicted polarization angles along different radial coordinates of the toroid for a parallel population. (c) Predicted polarization angles along different radial coordinates of the toroid for a perpendicular population.

of oligomers present at the modulation depth falloff. This is easily seen in Figure S10 where the number of number of chromophores at β , the 50% falloff, is invariant with the size of the nanocrystallite composing the particle within numerical error. Thus the estimated ~4000 oligomers associated with the modulation depth (crystallinity) falloff is robust to the model used.

3 Surface Orientation

Relating Surface Orientation to Toroidal Radial Coordinate The non-planar geometry of the toroidal resonator enables interrogation of spectral components perpendicular to the surface plane, although near field techniques²⁷ and defocused imaging²⁸ can circumvent this limitation on a planar substrate for emissive targets. If objects reside on the outer rim of the toroid, depicted in Figure S11a, then the population with a parallel dipole surface orientation, shown in green, would produce polarization angles tangential to the perimeter toroid (Figure S11b). This contrasts with a perpendicular dipole surface orientation, shown in blue, which would produce polarization angles orthogonal to the perimeter of the toroid (Figure S11c).

Comparing Different Observed Surface Orderings The observed trend in Main Text Figure 3c is reminiscent of the highly bimodal π -stacking direction preference seen via x-ray scattering, where populations of π -stacking direction were observed both perpendicular and parallel to the substrate.²⁹ However, these orientations can also be attributed to I) and II) respectively. The different measures of the anisotropic morphology of PEDOT:PSS require careful consideration of the possible surface orientations of the film. The three limiting cases of surface orientation are depicted in Figure S12 (center) and are helpful to understand the bimodal behaviors seen in π -stacking direction via microfocused grazing incidence wide-angle X-ray scattering²⁹ (left) and in this work (right), but it is important to remember that other orientations between these

limits may also be seen. In the bulk film the π -stacking surface orientation exhibits a bimodal distribution with both parallel (orange) and perpendicular (red) populations seen. This perpendicular population must originate from I), while the parallel orientation is ambiguous as it could arise from either II) or III). The bulk absorption probes the dipole surface orientation and predominantly finds absorption parallel to the substrate (green). This correlation suggests that the bulk is mostly comprised of I) and/or II) with negligible contribution of III). Taken together these two bulk measurements reveal populations of only I) and II). The bimodal distribution described in this work, however, clearly displays a significant amount of perpendicular dipole orientation

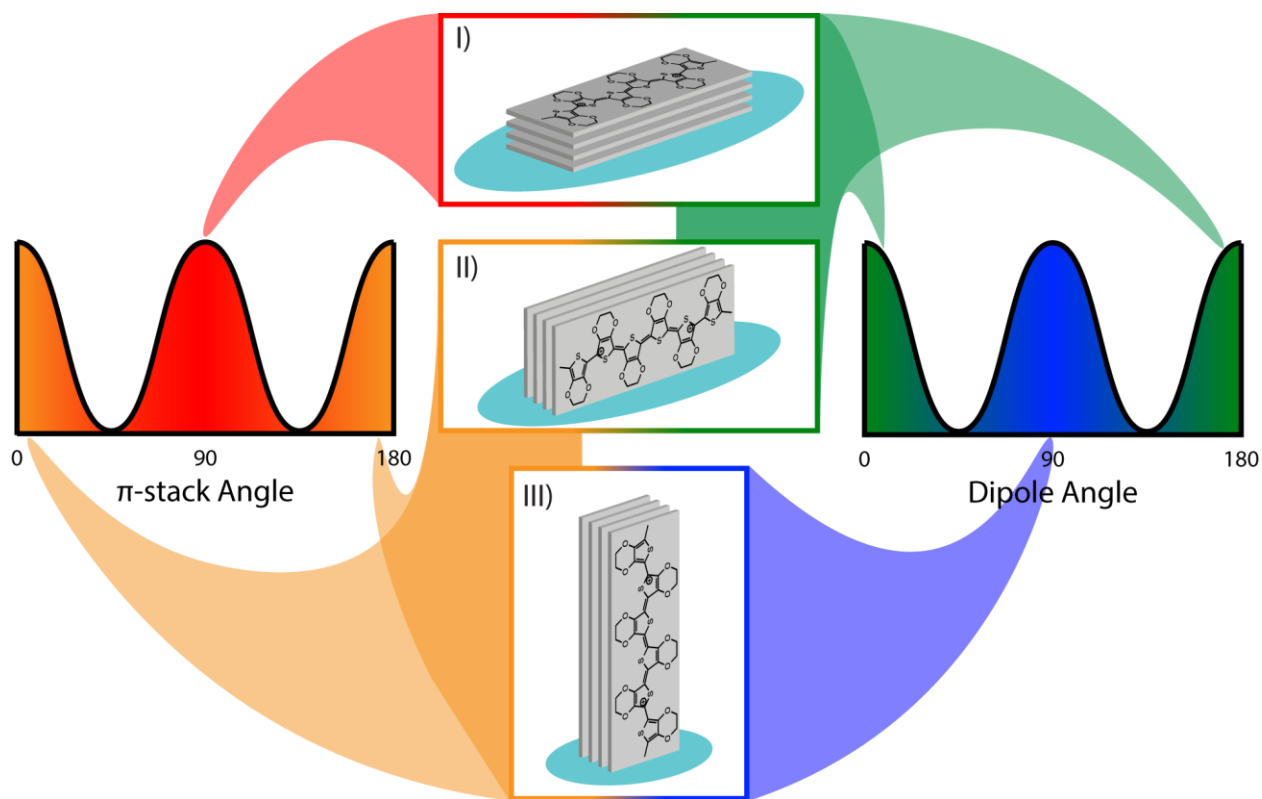


Figure S12: Surface orientation connection. Cartoon of the bimodal histogram of the π -stacking surface orientation angle from Ref. 18 (left) with the parallel population in orange and the perpendicular population in red. Cartoon of the bimodal histogram of dipole surface orientation angle from this work (right) with the parallel population in green and the perpendicular population in blue. The three limiting surface orientations (center) with their relative contribution to the π -stacking and dipole surface angle measurements color-coded in the outlining box and associated pointer.

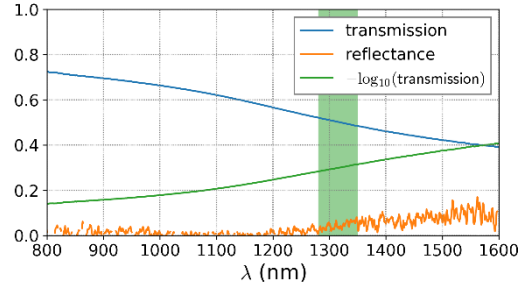


Figure S14: Thin film spectra. Transmission, reflectance, and extinction spectrum of the thin film used for ultrafast work. Extinction is calculated as $\log_{10}(\text{transmission})$.

(blue). Thus this measurement suggests that the layers closest to the surface are oriented differently than the bulk film as discussed in the Main Text.

4 Ultrafast Three Photon Echo Peak Shift Fitting

Thin Film Figure S13 shows the transmission, reflectance, and extinction spectrum of the thin film used in this work.

Experimental Geometry and Excitation Pulses Properties Continuously variable ND filters (THORLABS NDC-100C-4M, THORLABS NDL-10C-4) were used to ensure that all three excitation pulse powers were equal within measurement error.

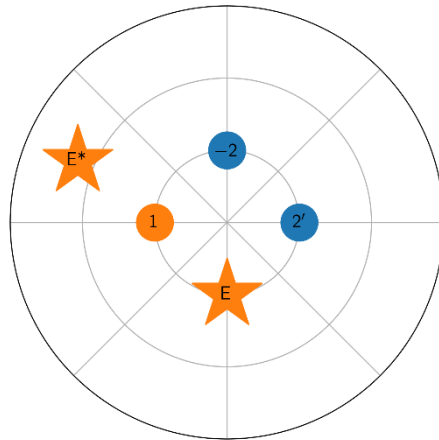


Figure S13: Phase matching mask. Phase matching mask used in this experiment. Each successive ring subtends 1 degree, such that the excitation pulses are each angled one degree relative to the mask center.

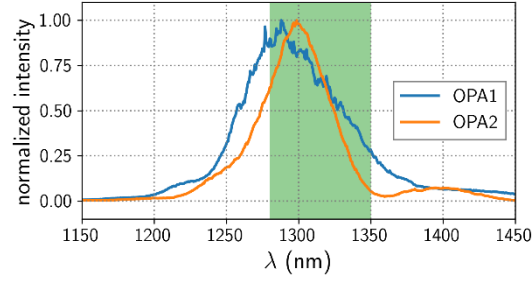


Figure S15: Excitation pulse spectra. Excitation pulse spectra of OPA1 (blue) and OPA2 (orange). The region explored in the single-particle absorption measurements is highlighted in green.

The angles between the three excitation beams were defined with a mask placed near the position of the focusing mirror. These angles created the phase matching required to create the E and E* output beams. Figure S14 shows the phase-matching mask used for these experiments. In this radial plot, each circular grid-line subtends a 1° angle at the sample. Each excitation pulse is shown as a colored circle. The two output beam (E and E*) directions are also shown as colored stars.

Figure S15 shows the spectrum of OPA1 and OPA2 used in these experiments. For comparison, the region explored using the microtoroid is highlighted in green.

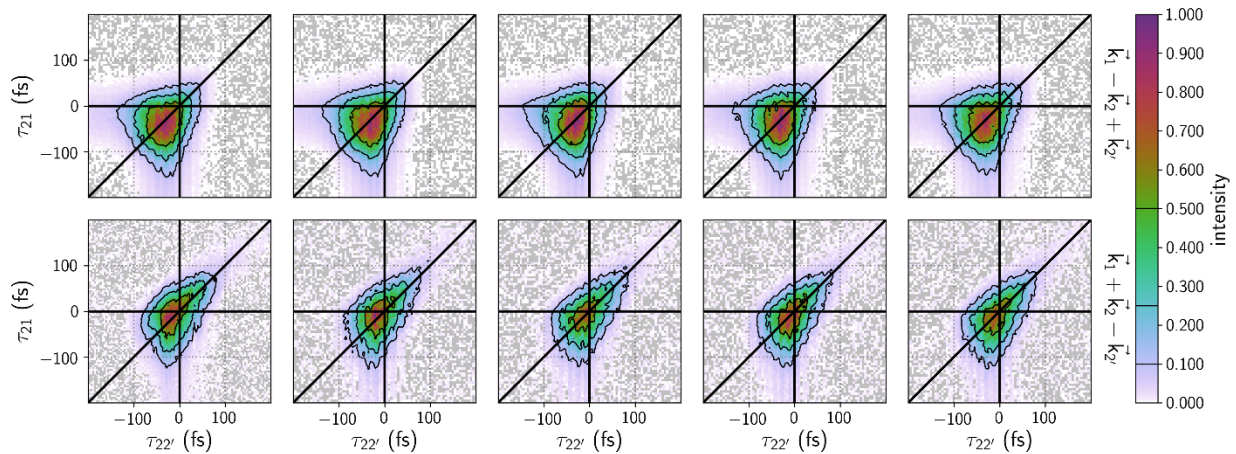


Figure S16: Raw ultrafast data. Unprocessed two-dimensional delay-delay plots. Each discrete acquisition is plotted as a single colored pixel. Grey pixels correspond to negative results, which appear in the no-signal regions due to noise.

The excitation beam waist was measured to be 375 μm FWHM by scanning a razor blade across the beam waist.

Raw Data For each phase matching condition, five experiments were collected at the same location on the same sample. All ten scans were taken over a single 24 hour period. Figure S16 shows these ten two-dimensional contour plots of the output intensity as a function of the delay-delay experiments in PEDOT:PSS. Each row of experiments shares the same colorbar to show the quantitative reproducibility.

Assignment of Zero Delay The absolute position of complete temporal overlap of the excitation pulses (zero delay) is a crucial step in determining the magnitude of the peak shift and therefore the total rephasing ability of the material. The strategy for assigning zero delay relies upon the intrinsic symmetry of the two-dimensional delay space. Figure S17 labels the six time-

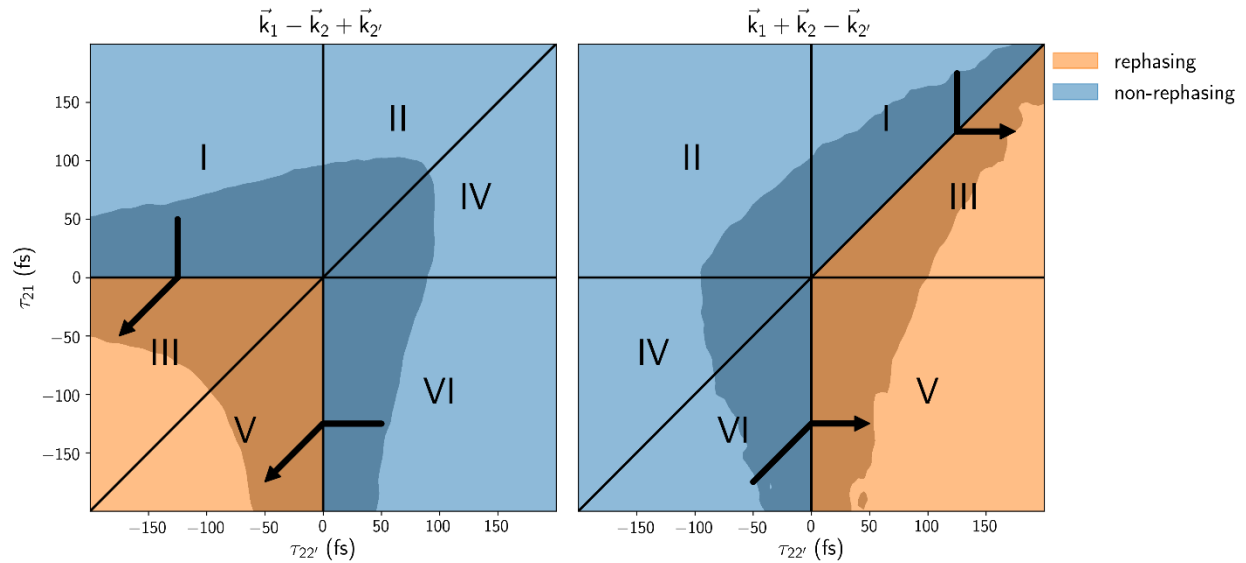


Figure S17: Representation of 2D delay space. Representation of symmetry between the two phase-matched experiments performed in this work. In each two-dimensional delay space, the six TOs are labeled. Pathways III and V are rephasing (orange), all other pathways are non-rephasing (blue). Thick black arrows are drawn along the τ trace for constant $T = 125$ fs, with arrowheads pointing in the direction of shift for positively correlated systems. The region with signal above 10% (processed dataset, amplitude level) is shaded to guide the eye

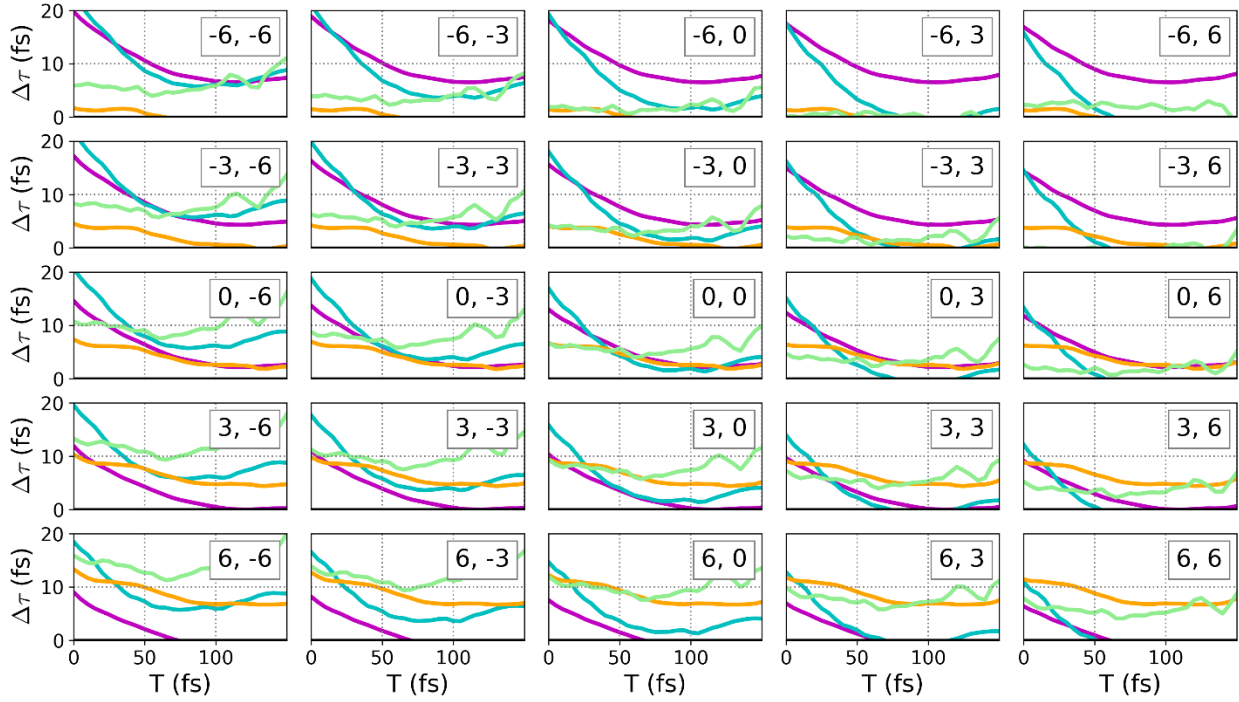


Figure S18: Delay offsets. Comparison between 3PEPS traces at different delay offsets.

orderings (TOs) of the three pulses that are possible with two delays. The TO labeling scheme follow from a convention first defined by Meyer, Wright, and Thompson.³⁰ Kohler et al first discussed how these TOs relate to traditional 3PE experiments.³¹ Briefly, spectral peaks shift into the rephasing TOs III and V when inhomogeneous broadening creates a photon echo in the III and V rephasing pathways colored orange in Figure S17. For both phase-matching conditions, there are two separate 3PE peak shift traces (represented as black arrows in Figure S17), yielding four different measurements of the photon echo. Since both 3PE and 3PE* were measured using the same alignment on the same day, the zero delay position is identical for the four photon echo measurements. We focus on this signature when assigning zero delay---zero is correct only when all four peak shifts agree. Conceptually, this is the two-dimensional analogue to the traditional strategy of placing zero such that the two conjugate peak shifts (3PE and 3PE*) agree.³²

We found that the 3PEPS traces agree best when the data in Figure S16 is offset by 19 fs in $\tau_{22'}$ and 4 fs in τ_{21} . Figure S18 shows the 3PEPS traces after correcting for the zero delay value. The entire 3PEPS trace (τ vs. T) is shown for regions I, III (purple and light green traces) and V, VI (yellow and and light blue traces) for the $\vec{k}_1 - \vec{k}_2 + \vec{k}_{2'}$ and $\vec{k}_1 + \vec{k}_2 - \vec{k}_{2'}$ phase matching conditions, respectively. Peak-shift magnitudes were found with Gaussian fits on the intensity level, in accordance with 3PEPS convention.³² The bottom subplot of Figure S18 shows the agreement between the four traces for $T > 50$ fs where pulse-overlap effects become negligible. These pulse-overlap effects cause the 3PEPS at small T even without inhomogeneous broadening.³² At long T , the average static 3PEPS is 2.5 fs. There is a deviation of the TO I-III

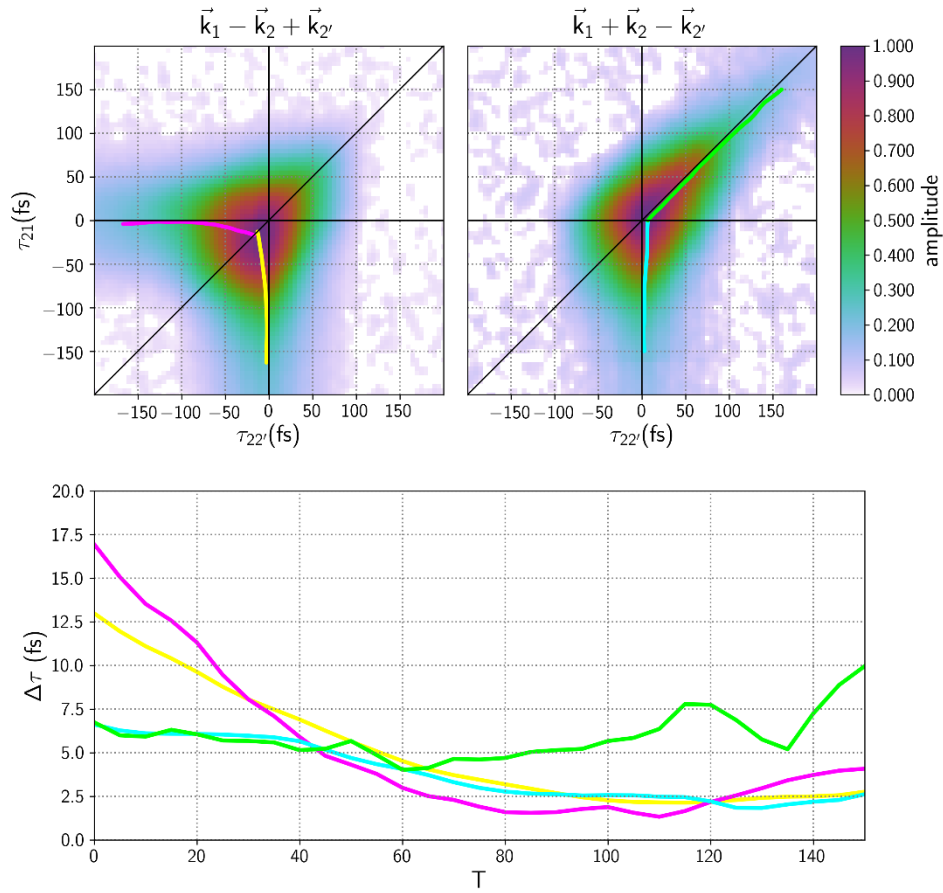


Figure S19: 3PEPS traces. Fully processed 2D delay scans (upper) and 3PEPS traces for both rephasing pathways and both phase matching conditions. The 3PEPS traces are shown mapped onto the 2D space (upper) and overlaid for comparison (lower).

Table S1: Fitted parameters for the coherent transient. The FWHM of the homogeneous line shape is $\hbar T_2^{-1}$.

Δ_t (fs)	T_2 (fs)	$\hbar T_2^{-1}$ (meV)	Δ_{inhom} (meV)
45	—	—	—
40	10	66	∞

3PEPS* trace (green line) from the other traces. It is attributed to a combination of excitation pulse distortions and line shape differences between OPA1 and OP2 and small errors in the zero delay correction (see Figure S15). Figure S19 shows what the four 3PEPS traces would look like for different choices of zero-delay. The inset numbers in each subplot denote the offset (from chosen zero) in each delay axis.

Numerical model We simulated the 3PEPS response of PEDOT:PSS through numerical integration of the Liouville-von Neumann Equation. Integration was performed on a homogeneous, three-level system with coherent dynamics described by

$$\frac{1}{T_2} = \frac{1}{2T_1} + \frac{1}{T_2^*} \quad (7)$$

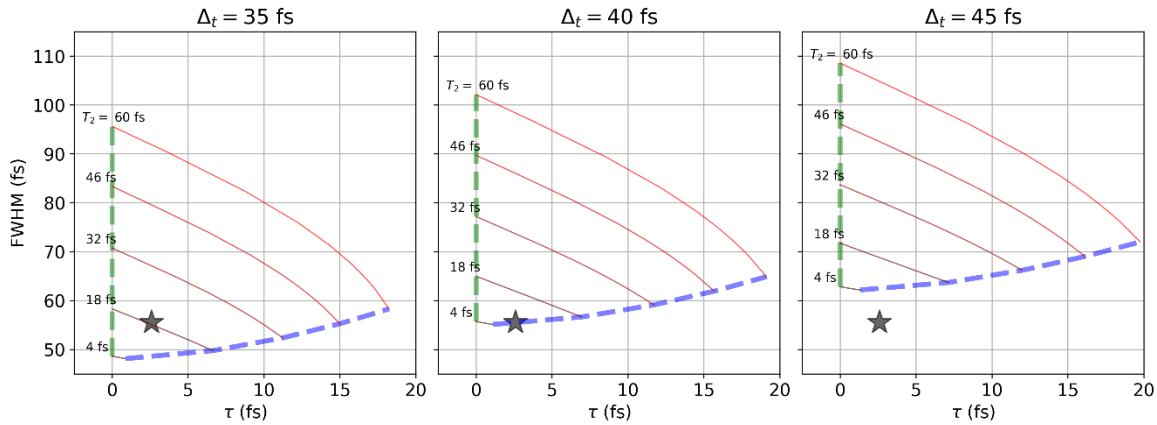


Figure S20: 3PEPS parameter space. Interplay of pure and ensemble dephasing on the coherent transient duration and the peak shift value for the three pulse-widths considered in Table S1. Red lines signify the parameters for constant values of T_2 and varying amounts of Δ_{inhom} . The domain of possible observables is bounded (blue hash for $\Delta_{\text{inhom}} \rightarrow \infty$, green hash for $\Delta_{\text{inhom}} = 0$). Also shown is the measured FWHM and peak shift from the PEDOT:PSS thin film (star).

where T_2 , T_1 , and T_2^* are the net dephasing, population relaxation, and pure dephasing rates, respectively. A three-level system was used because a two-level system cannot explain the population relaxation observed at long population times, T . This slow decay may be the same as the slowly decaying optical nonlinearities in PEDOT:PSS.³³ Inhomogeneity was incorporated by convolving the homogeneous response with a Gaussian distribution function of width Δ_{inhom} and allowing the resultant polarization to interfere on the amplitude level. This strategy captures rephasing peak shifts and ensemble dephasing.

It is difficult to determine the coherence dephasing and the inhomogeneous broadening using 3PE if both factors are large. To extract T_2^* and Δ_{inhom} , we focused on two key components of the dataset: coherence duration and peak shift at large T . Since dephasing is very fast in PEDOT:PSS we cannot directly resolve an exponential free induction decay. Instead, our model focuses on the FWHM of the τ trace to determine the coherence duration. At $T > 50$ fs, the transient

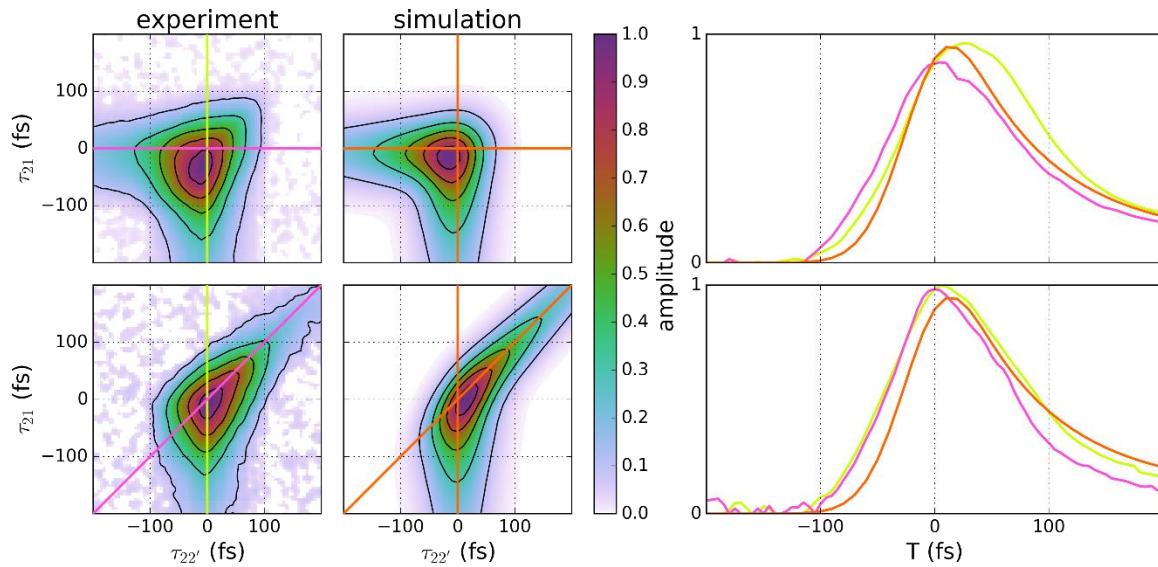


Figure S21: Agreement between simulation and experiment. Experiment and simulation in the full 2D representation (left) and transient grating slices (right), for both phase matching conditions (top and bottom). The identity of each slice can be inferred from its color. In this case the displayed simulation is for $\Delta t = 35$ fs, with the appropriate T_2 and Δ_{inhom} as seen in Table S1. Simulations for other pulse-widths look very similar.

has a FWHM of ~ 80 fs (intensity level). For comparison, our instrumental response is estimated to be 70-90 fs, depending on the exact value of our pulse duration Δ_t (35-45 FWHM, intensity level). An experimental peak shift of 2.5 fs was extracted using the strategy described above. Taken together, it is clear that both pure dephasing and ensemble dephasing influence FWHM and peak shift so it is important to find values of T_2^* and Δ_{inhom} that uniquely constrain the measured response.

We simulated the τ trace for a variety of Δ_{inhom} and T_2 values. The results for $\Delta_t = 40$ fs are summarized in Figure S20. The lines of constant T_2 span from $\Delta_{\text{inhom}} = 0$ (green left ends of curves) to the limit $\Delta_{\text{inhom}} \rightarrow \infty$ (blue right ends of curves). The lines of constant T_2 demonstrate that ensemble dephasing reduces the transient duration and introduces a peak shift. The influence of inhomogeneity on the observables vanishes as $T_2 \rightarrow \infty$.

We performed simulations analogous to those in Figure S20 for pulse durations larger and smaller than $\Delta_t = 40$ fs. Longer pulse durations create solutions that do not intersect our experimental point (see right-most subplot of Figure S20), but shorter pulse durations do. Table S1 summarizes the coherence dephasing time and inhomogeneous broadening values that best matches the experimental FWHM and inhomogeneous broadening value for $\Delta_t = 35, 40$, and 45 fs. Clearly, there is no upper limit that can provide an upper limit for the inhomogeneous broadening.

Our model system does an excellent job of reproducing the entire 2D transient within measurement error (Figure S21). The most dramatic disagreement is in the upper right, where the experiment decays much slower than the simulation. Our system description does not account for signal contributions in TOs II and IV double quantum coherence resonances are important. In

addition, excitation pulse shapes may cause such distortions. Regardless, these contributions do not affect our analysis.

Extremely fast (single fs) carrier scattering time constants have also been observed for PEDOT-based conductive films.³⁴⁻³⁶

The raw data, scripts, and custom simulation package used in the analysis of the ultrafast spectra presented in this work are publicly available for download from the Open Science Framework (OSF) [DOI:10.17605/OSF.IO/BS8PR](https://doi.org/10.17605/OSF.IO/BS8PR). They are permissively licensed for reuse and modification. Our simulations and processing tools are built on top of the open source, publicly available Scientific Python ecosystem, and can be edited and executed without access to special computing resources. Further details can be found in the OSF repository.

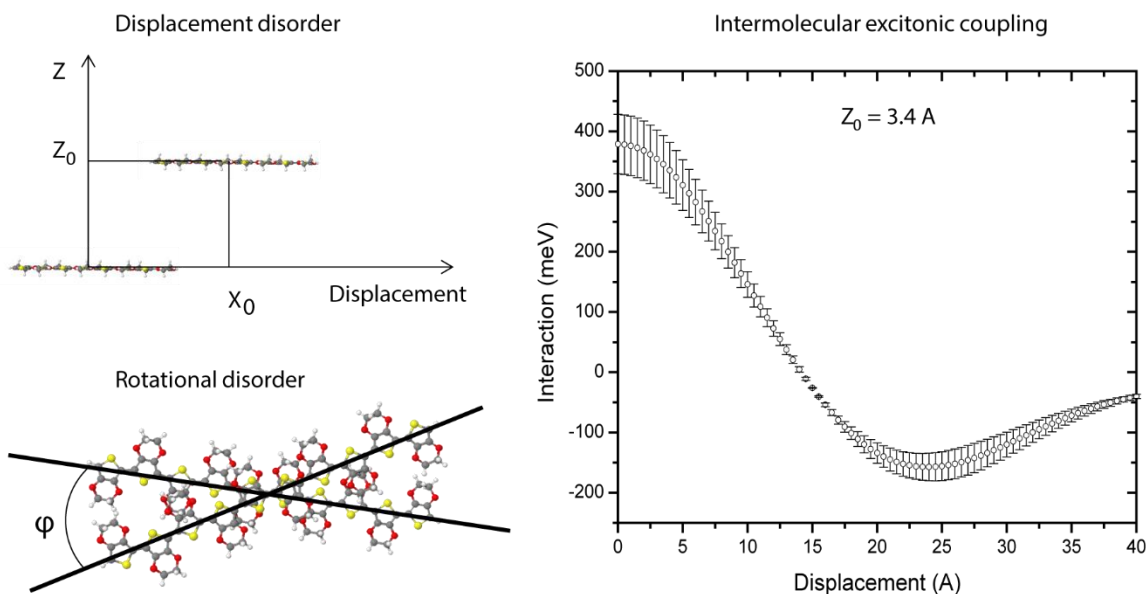


Figure S22: Excitonic interaction in an oligomer dimer. Left: A relative alignment of two PEDOT oligomers. Two types of the structural disorder are introduced. Right: Excitonic (Förster) interaction between nearest neighbor oligomers as a function of a relative displacement. The error bar shows a variation of the interaction due to relative rotation of the oligomers about z-axis within the range -10 – 10 degrees.

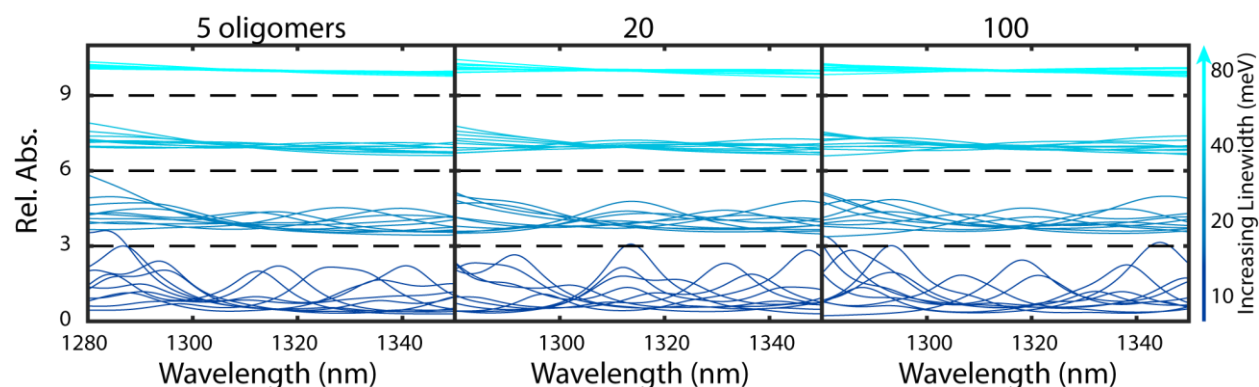


Figure S23: Superrealization absorption spectra. Absorption spectrum for single super realizations of chains with length 5 (left), 20 (middle) and 100 (right) oligomers. Each color represents a different broadening: 10 meV (lower dark blue), 20 meV, 40 meV and 80 meV (highest light blue). Ten absorption spectra are plotted for each case.

5 Electronic Structure Calculations

We introduce a structural disorder into the chain model by allowing a parallel displacement and small relative rotations between neighboring oligomers as illustrated in the left panel of Figure S22. In particular, the maximal value of parallel displacement was limited to 5 monomers, which is a half of the oligomer length. Larger values of structural disorder were studied previously.³⁷

Then, we computed interactions between single oligomers in the chains using electron transition densities of oligomer dimers as described previously.³⁸ The right panel of Figure S22 shows the displacement dependence of the intermolecular couplings for two nearest neighbor oligomers (the distance $Z_0 = 3.4$ Angstroms). The error bar in Figure S22 shows the variation of the couplings due to a relative rotation $\pm 10^\circ$ from coalignment, (ϕ , Figure S22a, bottom). As one can see, the effect of the rotational disorder on the intermolecular coupling is small compared to the disorder due to the molecular displacement and can be ignored in our simulation. Therefore, for spectral characterization we focused on the displacement contribution only.

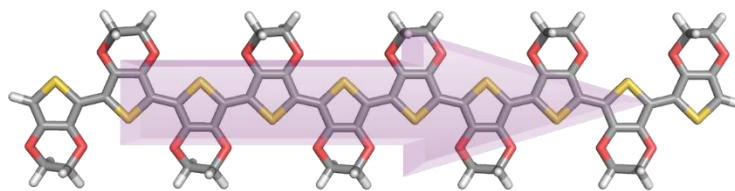


Figure 24: Bipolaron transition dipole of PEDOT 10mer.

The structural displacement disorder allows the creation of different chain realizations. We fixed the number of total oligomers to 100, what we termed a single super-realization, and studied three different cases: i) a single randomly generated chain of 100 oligomers length; ii) 5 randomly generated chains of 20 oligomers length; and 20 randomly generated chains of 5 oligomers length. As can be seen from Figure S23, it is not possible to determine the chain length from these measurements.

The orientation of the transition dipole of the bipolaron relative to the PEDOT oligomer backbone was examined using a single doubly charged PEDOT 10mer. We calculated the 5 lowest electronic excitations in this species using TDDFT as implemented in Turbomole 6.0.³⁷ The computed transition dipole associated with the lowest electronic excitation, which has the largest oscillator strength, is parallel to the main axis of the oligomer, Figure S24.

References

1. van de Ruit, K.; Cohen, R. I.; Bollen, D.; van Mol, T.; Yerushalmi-Rozen, R.; Janssen, R. A. J.; Kemerink, M. *Adv. Funct. Mater.* **2013**, 23, 5778-5786.
2. Samitsu, S.; Shimomura, T.; Ito, K.; Fujimori, M.; Heike, S.; Hashizume, T. *Appl. Phys. Lett.* **2005**, 86, 233103
3. Kim, N.; Kee, S.; Lee, S. H.; Lee, B. H.; Kahng, Y. H.; Jo, Y. R.; Kim, B. J.; Lee, K. *Adv. Mater.* **2014**, 26, 2268-2272.
4. Crispin, X.; Jakobsson, F. L. E.; Crispin, A.; Grim, P. C. M.; Andersson, P.; Volodin, A.; van Haesendonck, C.; Van der Auweraer, M.; Salaneck, W. R.; Berggren, M. *Chem. Mater.* **2006**, 18, 4354-4360.
5. Kim, Y. H.; Sachse, C.; Machala, M. L.; May, C.; Muller-Meskamp, L.; Leo, K. *Adv. Funct. Mater.* **2011**, 21, 1076-1081.

6. DeLongchamp, D. M.; Vogt, B. D.; Brooks, C. M.; Kano, K.; Obrzut, J.; Richter, C. A.; Kirillov, O. A.; Lin, E. K. *Langmuir* **2005**, *21*, 11480-11483.
7. Lang, U.; Muller, E.; Naujoks, N.; Dual, J. *Adv. Funct. Mater.* **2009**, *19*, 1215-1220.
8. Greco, F.; Zucca, A.; Taccola, S.; Menciassi, A.; Fujie, T.; Haniuda, H.; Takeoka, S.; Dario, P.; Mattoli, V. *Soft Matter* **2011**, *7*, 10642-10650.
9. Heylman, K. D.; Thakkar, N.; Horak, E. H.; Quillin, S. C.; Cherqui, C.; Knapper, K. A.; Masiello, D. J.; Goldsmith, R. H. *Nat. Photon.* **2016**, *10*, 788-795.
10. Wang, C. C.; Duong, D. T.; Vandewal, K.; Rivnay, J.; Salleo, A. *Phys. Rev. B* **2015**, *91*, 119901.
11. Zotti, G.; Zecchin, S.; Schiavon, G.; Louwet, F.; Groenendaal, L.; Crispin, X.; Osikowicz, W.; Salaneck, W.; Fahlman, M. *Macromolecules* **2003**, *36*, 3337-3344.
12. Celebrano, M.; Kukura, P.; Renn, A.; Sandoghdar, V. *Nat. Photon.* **2011**, *5*, 95-98.
13. Kirchmeyer, S.; Reuter, K. *J. Mater. Chem.* **2005**, *15*, 2077-2088.
14. Rivnay, J.; Inal, S.; Collins, B. A.; Sessolo, M.; Stavrinidou, E.; Strakosas, X.; Tassone, C.; DeLongchamp, D. M.; Malliaras, G. G. *Nat. Commun.* **2016**, *7*, 11287.
15. Ouyang, L. Q.; Musumeci, C.; Jafari, M. J.; Ederth, T.; Inganas, O. *ACS Appl. Mater. Interfaces* **2015**, *7*, 19764-19773.
16. Brown, P. J.; Sirringhaus, H.; Harrison, M.; Shkunov, M.; Friend, R. H. *Phys. Rev. B* **2001**, *63*, 125204.
17. Yokonuma, N.; Furukawa, Y.; Tasumi, M.; Kuroda, M.; Nakayama, J. *Chem. Phys. Lett.* **1996**, *255*, 431-436.
18. Ouyang, J.; Xu, Q. F.; Chu, C. W.; Yang, Y.; Li, G.; Shinar, J. *Polymer* **2004**, *45*, 8443-8450.
19. Lu, H. P.; Xie, X. S. *Nature* **1997**, *385*, 143-146.
20. Meixner, A. J.; Weber, M. A. *J. Lumin.* **2000**, *86*, 181-187.
21. Blum, C.; Stracke, F.; Becker, S.; Mullen, K.; Meixner, A. J. *J. Phys. Chem. A* **2001**, *105*, 6983-6990.
22. Nicolet, A. A. L.; Kol'chenko, M. A.; Hofmann, C.; Kozankiewicz, B.; Orrit, M. *Phys. Chem. Chem. Phys.* **2013**, *15*, 4415-4421.
23. Wilma, K.; Issac, A.; Chen, Z. J.; Wurthner, F.; Hildner, R.; Kohler, J. *J. Phys. Chem. Lett.* **2016**, *7*, 1478-1483.
24. Rutledge, S. A.; Helmy, A. S. *J. Appl. Phys.* **2013**, *114*, 133708.
25. Yan, F.; Parrott, E. P. J.; Ung, B. S. Y.; Pickwell-MacPherson, E. J. *Phys. Chem. C* **2015**, *119*, 6813-6818.
26. Hunter, G. L.; Edmond, K. V.; Elsesser, M. T.; Weeks, E. R. *Opt. Express* **2011**, *19*, 17189-17202.
27. Betzig, E.; Chichester, R. J. *Science* **1993**, *262*, 1422-1425.
28. Sick, B.; Hecht, B.; Novotny, L. *Phys. Rev. Lett.* **2000**, *85*, 4482-4485.
29. Palumbiny, C. M.; Heller, C.; Schaffer, C. J.; Korstgens, V.; Santoro, G.; Roth, S. V.; Muller-Buschbaum, P. *J. Phys. Chem. C* **2014**, *118*, 13598-13606.
30. Meyer, K. A.; Wright, J. C.; Thompson, D. E. *J. Phys. Chem. A* **2004**, *108*, 11485-11493.
31. Kohler, D. D.; Block, S. B.; Kain, S.; Pakoulev, A. V.; Wright, J. C. *J. Phys. Chem. C* **2014**, *118*, 5020-5031.
32. Weiner, A. M.; Desilvestri, S.; Ippen, E. P. *J. Opt. Soc. Am. B* **1985**, *2*, 654-662.
33. Meskers, S. C. J.; van Duren, J. K. J.; Janssen, R. A. J. *Adv. Funct. Mater.* **2003**, *13*, 805-810.
34. Chang, Y. H.; Lee, K.; Kiebooms, R.; Aleshin, A.; Heeger, A. J. *Synth. Met.* **1999**, *105*, 203-206.
35. Cho, S.; Park, S. H.; Lee, K. *J. Korean Phys. Soc.* **2005**, *47*, 474-478.
36. Zhuo, J. M.; Zhao, L. H.; Chia, P. J.; Sim, W. S.; Friend, R. H.; Ho, P. K. H. *Phys. Rev. Lett.* **2008**, *100*, 186601.
37. Gelbwaser-Klimovsky, D.; Saikin, S. K.; Goldsmith, R. H.; Aspuru-Guzik, A. *ACS Energy Lett.* **2016**, *1*, 1100-1105.

38. Valteau, S.; Saikin, S. K.; Yung, M. H.; Guzik, A. A. *J. Chem. Phys.* **2012**, 137, 034109